nature astronomy

Article

https://doi.org/10.1038/s41550-022-01837-2

Measured spin-orbit alignment of ultra-short-period super-Earth 55 Cancri e

Received: 10 June 2022

Accepted: 20 October 2022

Published online: 08 December 2022



Check for updates

Lily L. Zhao © 1 ⋈, Vedad Kunovac © 2, John M. Brewer 3, Joe Llama 2, Sarah C. Millholland ⁴, Christina Hedges^{5,6}, Andrew E. Szymkowiak ^{7,8}, Rachael M. Roettenbacher^{7,9}, Samuel H. C. Cabot⁷, Sam A. Weiss⁷ & Debra A. Fischer⁷

A planet's orbital alignment places important constraints on how a planet formed and consequently evolved. The dominant formation pathway of ultra-short-period planets (P < 1 day) is particularly mysterious as such planets most likely formed further out, and it is not well understood what drove their migration inwards to their current positions. Measuring the orbital alignment is difficult for smaller super-Earth/sub-Neptune planets, which give rise to smaller amplitude signals. Here we present radial velocities across two transits of 55 Cancri (Cnc) e, an ultra-short-period super-Earth, observed with the Extreme Precision Spectrograph, Using the classical Rossiter-McLaughlin method, we measure 55 Cnc e's sky-projected stellar spin-orbit alignment (that is, the projected angle between the planet's orbital axis and its host star's spin axis) to be $\lambda = 10 {+17 \choose -20}$ with an unprojected angle of $\psi = 23^{+14^{\circ}}_{-12^{\circ}}$. The best-fit Rossiter–McLaughlin model to the Extreme Precision Spectrograph data has a radial velocity semiamplitude of just $0.41^{+0.09}_{-0.10}$ m s⁻¹. The spin–orbit alignment of 55 Cnc e favours dynamically gentle migration theories for ultra-short-period planets, namely tidal dissipation through low-eccentricity planet-planet interactions and/or planetary obliquity tides.

The star 55 Cancri (Cnc) A hosts five known exoplanets with minimum mass estimates ranging from approximately $8M_{\oplus}$ to $3M_{\text{lun}}$ and periods less than one day to nearly 20 years¹⁻⁴. Of particular interest has been 55 Cnc e, one of the most massive known ultra-short-period planets (USPs) and the only planet around 55 Cnc found to transit^{5,6}. It has an orbital period of $0.7365474^{+1.3}_{-1.4}\times10^{-6}_{-1.4}\times10^{-6}_{-1.4}$ and a radius of $1.853^{+0.026}_{-0.027}$ R_{\oplus} (refs. ^{7,8}). A precise measure of the stellar spin-orbit alignment of 55 Cnc e-the angle between the host

star's spin axis and the planet's orbit normal—will shed light on the formation and evolution of USPs, especially in the case of compact, multiplanet systems.

It has been shown that USPs form a statistically distinct population of planets9 that tend to be misaligned with other planetary orbits in their system¹⁰. This suggests that USPs experience a unique migration pathway that brings them close in to their host stars. This inward migration is most likely driven by dissipation due to star-planet tidal interactions that result from either non-zero eccentricities 11,12 or planetary spin-axis tilts¹³.

¹Center for Computational Astrophysics, Flatiron Institute, Simons Foundation, New York, NY, USA. ²Lowell Observatory, Flagstaff, AZ, USA. ³Department of Physics & Astronomy, San Francisco State University, San Francisco, CA, USA. 4MIT Kavli Institute for Astrophysics and Space Research, Massachusetts Institute of Technology, Cambridge, MA, USA. 5University of Maryland, Baltimore County, Baltimore, MD, USA. 6NASA Goddard Space Flight Center, Greenbelt, MD, USA. 7Department of Astronomy, Yale University, New Haven, CT, USA. 8Department of Physics, Yale University, New Haven, CT, USA. ⁹Department of Astronomy, University of Michigan, Ann Arbor, MI, USA. ⊠e-mail: lzhao@flatironinstitute.org

The stellar spin-orbit alignment of a transiting planet can be measured by obtaining spectroscopic observations during the planet's transit, Commonly called the Rossiter-McLaughlin (RM) effect 14,15 radial velocity (RV) deviations as a planet transits a rotating star reveal whether the planet is transiting across the blueshifted half of the star that rotates towards the observer or the redshifted half of the star that rotates away. Capturing the resultant net red/blueshift reveals the orientation of the planet's orbital normal vector with respect to its host star's spin vector, that is, the sky-projected stellar spin-orbit alignment or the stellar obliquity.

Previous attempts to measure the RM effect for 55 Cnc e have produced mixed results. Using data from the High Accuracy Radial velocity Planet Searcher for the Northern hemisphere (HARPS-N),

Bourrier et al. ¹⁶ reported a sky-projected obliquity of $\lambda = 72 + 13^{\circ}$.

However, the best-fit model from that analysis also returned a stellar projected rotational velocity of $v \sin i_{+} = 3.3 \pm 0.9 \text{ km s}^{-1}$, which is not consistent with the stellar projected equatorial velocity, $v \sin i_{\star}$, measured by other studies8. A separate observing campaign also using HARPS-N data reported a non-detection, concluding that given the quality of their data the RM signal generated by 55 Cnc e must have an amplitude less than ~35 cm s $^{-1}$ (ref. 17).

In this Article we present a 41 $^{+9}$ cm s $^{-1}$ amplitude RM detection

of 55 Cnc e using observations from the Extreme Precision Spectrograph (EXPRES). The arrival of ultra-stabilized spectrographs, including EXPRES and ESPRESSO among others, have made sub-metre-per-second RV precision possible 18,19. This measurement is the smallest amplitude classic RM detection so far. Precision RV measurements from spectrographs such as EXPRES will be able to detect lower-amplitude RM effects that have previously been missed in the regime of small planets or slowly rotating stars.

Results

We use two sectors of photometry from the Transiting Exoplanet Survey Satellite (TESS) to fit for the transit parameters of 55 Cnc e, which are then used to constrain the RM model. We use RV measurements from EXPRES to detect and fit for the RM effect during two 55 Cnc e transits observed on 31 January 2022 and 6 April 2022. The EXPRES spectra were also used to derive stellar properties for 55 Cnc using Spectroscopy Made Easy (SME)^{20,21}.

The EXPRES RVs and RM fits are shown in Fig. 1. The best-fit RM models for each individual night as well as the combined data are plotted over the EXPRES data in yellow with darker and lighter shading showing the 50th and 90th percentiles of the posterior distribution, respectively. The full posterior distribution was sampled using a Markov chain Monte Carlo (MCMC) method.

With the combined fit using both nights of observations, we find that 55 Cnc e has a sky-projected stellar obliquity of $\lambda = 10 {+17^{\circ} \atop -20^{\circ}}$. By incorporating the rotation period of 55 Cnc⁸ we derive an unprojected stellar obliquity of $\psi=23^{+14^{\circ}}_{-12^{\circ}}$. We therefore find that the orbit normal of 55 Cnc e is close to aligned with its host star's rotation axis. The best-fit transit and RM parameters are given in Table 1 along with the priors used in the fitting. Other nuisance parameters needed for each fit as well as the results of the fits to each individual night are given in Table 2 and described more fully in the Methods below. The measured stellar spin-orbit alignment of 55 Cnc e is graphically represented in Fig. 2.

Discussion

We recover a statistically significant detection of the RM effect for 55 Cnc e using EXPRES data with a false alarm probability of 0.3%.

The amplitude of the measured signal, $K_{\rm RM} = 0.41 {+0.09 \atop -0.10} \, {\rm m \, s^{-1}}$, is the

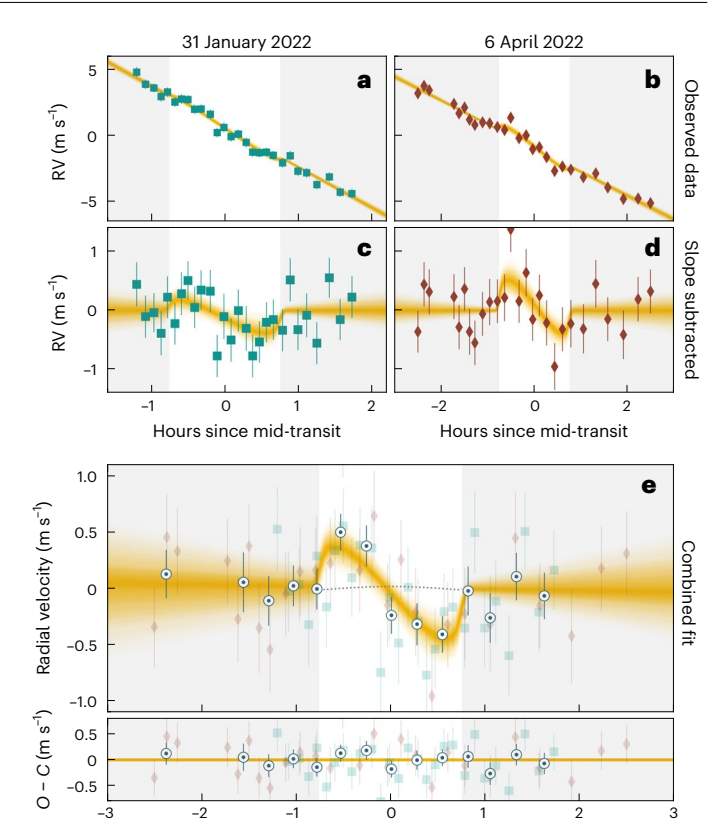


Fig. 1 | RM model fit to two nights of EXPRES RV data. Data from 31 January 2022 are shown as green squares and 6 April 2022 as red diamonds. The RV value (indicated by each marker) represents the best-fit Doppler shift produced by the EXPRES chunk-by-chunk, forward modelling pipeline with error bars spanning the corresponding 1σ errors (see ref. ⁴⁵ for more information on the EXPRES pipeline). RM models are shown as yellow curves. Shaded yellow regions span 50th to 99th percentiles of the posterior sampled by the MCMC method. The white highlighted area spans the transit duration of 55 Cnc e. a-d, Plots of each of the two nights of observations for 31 January 2022 (a,c) and 6 April 2022 (b,d). a,b, The original RVs along with the full model fit for each night. c,d, The RVs and model fit with the best-fit linear slope removed. e, The combined fit to both nights of data and the residuals to the best fit. White circular points represent both nights of data binned by phase with points every 0.015 phase units (~15.9 min) to help guide the eye. Phase binned points are calculated as the average of all data points within the phase bin weighted by their errors, σ_i , with associated errors given by $\sqrt{1/(\sum 1/\sigma_i^2)}$. The dotted grey line represents the centre-to-limb convective blueshift contribution to the RVs, which has a semi-amplitude of 1.3 cm s⁻¹.

Hours since mid-transit

smallest classically recovered RM measurement so far. Two other super-Earth systems have similar expected RM amplitudes, but can only be detected using stellar line profile analysis^{22,23}

This result clarifies previous measurements of 55 Cnc e's stellar spin-orbit alignment, which gave contradictory results 16,17. Bourrier et al. 16 previously reported best-fit RM values of $\lambda = 72 \, ^{+13^{\circ}}_{-12^{\circ}}$ and $v \sin i_{\star} = 3.3 \pm 0.9 \text{ km s}^{-1}$. This $v \sin i_{\star}$ value is ~1.8 σ greater than the literature value derived from stellar line broadening, which reports the $v \sin i_{\star}$ as 1.7 ± 0.5 km s⁻¹ (ref. ²⁰). The RM fit presented here returns a best-fit $v \sin i_{\star}$ of 2.00 $^{+0.43}_{-0.47}$ km s⁻¹, which is within 1σ agreement of the literature value. Our RM fit additionally agrees with the independent SME line broadening analysis, which returned a $v \sin i_{\star}$ of 1.94 \pm 0.50 km s⁻¹. These $v \sin i_{\star}$ values are in some tension with the rotational velocity calculated using the stellar radius and rotation period ($v = \frac{2\pi R_{\star}}{P_{\star}} = 1.23 \pm 0.01 \text{km s}^{-1}$) by -1.5 σ . However, the agreement

Table 1 | 55 Cnc e fit parameters

Parameter	Symbol	Value	Unit	Prior
Transit fit				
Planet/star radii ratio	$R_{\rm p}/R_{\star}$	$0.018016 ^{+0.000085}_{-0.000077}$		LogNormal(-8,10)
Planet radius	R _p	1.856 ^{+0.024} -0.025	R_{\oplus}	-
Orbital period	Р	0.7365430±0.0000014	days	Normal(0.736546,1)
Transit epoch	T_{o}	$2,459,511.487987 ^{+0.000071}_{-0.000075}$	BJD_TDB	Normal(2,459,511.48778,1)
Impact parameter	b	$0.373^{+0.027}_{-0.032}$	R _*	Uniform(0,1)
Orbital inclination	i	83.9 ^{+0.6} _{-0.5} °		-
Orbital separation	a/R _*	$3.516^{+0.042}_{-0.041}$		-
Transit duration	T ₁₄	1.5439 +0.0027 hours -0.0026		-
Limb-darkening	<i>u</i> ₁	0.4823±0.0017		Normal(0.4824, 0.0017)
	U ₂	$0.1276^{+0.0037}_{-0.0041}$		Normal(0.1280, 0.0038)
RM fit				
Fitted parameters				
Sky-projected obliquity	λ	10 ⁺¹⁷ ₋₂₀	0	Uniform(-180°,180°)
Projected rotational velocity	v sin i⋆	2.00 ^{+0.43} _{-0.47}	kms ⁻¹	Uniform(0,18)
Net convective blueshift velocity	V _{CB}	-157 ⁺⁸⁶ -94	ms ⁻¹	Uniform(-1000,0), Normal(-150,100)
Derived parameters				
RM semi-amplitude	K_{RM}	$0.41^{+0.09}_{-0.10}$	ms ⁻¹	
Stellar inclination	i _*	75 ⁺¹¹ °		
Obliquity	Ψ	23 ⁺¹⁵ ₋₁₂	0	

between the two methods used here as well as agreement with literature values 20,24 suggests this is due to uncertainties in the quoted rotation period possibly because of differential rotation or spots.

The EXPRES data used in this analysis have a consistent and often a higher signal-to-noise ratio (SNR) as well as lower uncertainties than the RV measurements previously used. All EXPRES observations were integrated until they reached a constant SNR of 225 at 550 nm; this consistency in SNR allowed for more stable final RVs with similar error properties. Although it is difficult to compare SNRs between different spectrographs given each instrument's unique throughput response as a function of wavelength, we report that López-Morales et al.¹⁷ used observations that ranged in SNR between 100 and 275 with a median SNR of 165 at 624 nm. Bourrier et al. 16 give a median SNR across all nights of 144 at 527 nm with the median SNR within a night ranging from 92 to 354. The HARPS-N RVs previously used have a median error of about 80 cm s⁻¹ and were calibrated using either a ThAr lamp or a Fabry-Pérot etalon while the EXPRES RVs have a median error of 38 cm s⁻¹ and are calibrated using a laser frequency comb. The EXPRES observations are more stable, have smaller RV uncertainties and return a best-fit RM model more aligned with literature values than previous attempts at measuring 55 Cnc e's stellar spin-orbit alignment.

With this robust measurement using EXPRES data, we can place constraints on the different proposed dynamical histories for the 55 Cnc system. Studies have suggested that owing to 55 Cnc's distant stellar companion, one would expect all the planets around 55 Cnc to precess as a rigid plane around the host star, resulting in all planets sharing a common planetary orbit axis that is misaligned with respect to the host star's spin axis²⁵. Other simulations propose that secular resonances between 55 Cnc e and the other planets in the system led to excitation of 55 Cnc e's eccentricity and inclination, causing 55 Cnc e's orbital axis to be misaligned with the other planets' orbital axes as well as the host star's spin axis²⁶. Analysis using the system's precession frequencies²⁷, on the other hand, finds that one would expect to find 55 Cnc e's orbital axis closer to aligned with its host star's spin axis²⁸, which is what our measurement shows.

Various theories for the migration pathways of USPs differ in terms of the predicted spin-orbit alignments. Secular planet-planet interactions have been shown to give rise to tidal dissipation inside the planets and can operate under both high-eccentricity and low-eccentricity modes. The high-eccentricity mode leads to excitation of planetary eccentricities and inclinations through secular chaos, resulting in generally misaligned systems with large stellar spin-orbit alignment angles and USPs whose orbits have decayed to close-in, circular orbits ¹¹.

Table 2 | TESS and EXPRES fitted nuisance parameters

Parameter	Symbol	Value	Unit	Prior
TESS fit				
Sector 44				
GP amplitude	$\sigma_{ ext{GP}}$	$0.234_{-0.022}^{+0.028}$	ppt	LogNormal(-8,10)
GP timescale	$ au_{ ext{GP}}$	$1.086^{\ +0.135}_{\ -0.105}$	day	LogNormal(2,10)
Mean flux	f	0.045±0.035	ppt	Normal(0,10)
White noise	σ	0.0980±0.0012	ppt	LogNormal(-16,10)
Sector 46				
GP amplitude	$\sigma_{ ext{GP}}$	$0.112^{+0.016}_{-0.013}$	ppt	LogNormal(-8,10)
GP timescale	$ au_{GP}$	$2.22^{+0.32}_{-0.23}$	day	LogNormal(2,10)
Mean flux	f	$0.018^{+0.022}_{-0.021}$	ppt	Normal(0,10)
White noise	σ	$0.0965^{+0.0011}_{-0.0012}$	ppt	LogNormal(-16,10)
EXPRES fit				
31 January 2022				
Sky-projected obliquity	λ	34 ⁺²⁴ ₋₂₆	•	Uniform(–180°,180°)
Projected rotational velocity	vsini _⋆	$1.74^{+0.62}_{-0.68}$	km s ⁻¹	Uniform(0,18)
Intercept	y ₀	$0.646^{+0.034}_{-0.033}$	ms ⁻¹	-
Slope	т	-72.4 ^{+2.0} -2.1	ms ⁻¹ day ⁻¹	Uniform(-150, -50)
6 April 2022				
Sky-projected obliquity	λ	-19 ⁺³⁰ ₋₂₀	o	Uniform(-180°,180°)
Projected rotational velocity	v sin i⋆	2.36 ^{+0.59} _{-0.65}	kms ⁻¹	Uniform(0,18)
Intercept	y ₀	$-0.952^{+0.023}_{-0.022}$	ms ⁻¹	-
Slope	m	-43.1 ^{+1.4} _{-1.3}	ms ⁻¹ day ⁻¹	Uniform(-150, -5)

The given uncertainties represent each measurement's 68% credible interval. ppt, parts per 10^3 .

Planet–planet interactions can also lead to the inward migration of planets even in the case of modest eccentricities¹². This mechanism is less chaotic and probably results in USP orbits that are aligned to within a few tens of degrees.

Planetary obliquity tides have also been proposed as a source for tidal dissipation of USPs¹³. Here planetary obliquity is used to refer to the angle between the planet's spin axis and the planet's orbital plane (as opposed to the stellar obliquity). Planetary-obliquity-driven tidal dissipation has no requirements on the initial planet eccentricities. This mechanism predicts that a planet's orbit normal will become closer to aligned with the host star's spin axis as it migrates inwards but may be misaligned with the orbit normals of other planets in the system.

The close alignment of 55 Cnc e's orbit normal with its host star's stellar axis preliminarily favours the low eccentricity¹² and planetary obliquity¹³ tide models. It is of particular interest that 55 Cnc e is the only planet of the five known planets around 55 Cnc that transits. This suggests that though 55 Cnc e's orbit normal is aligned with the spin axis of its host star, it is possibly misaligned from those of the other

planets. This is expected from the planetary obliquity tides model if there existed some primordial misalignment of the stellar obliquity, for example due to 55 Cnc's distant binary companion²⁵.

In the scenario with an initial misalignment, 55 Cnc e may have formed out of the protoplanetary disk with an orbital plane aligned with the outer planets, but as it migrated inwards, 55 Cnc e became more influenced by the gravitational quadrupole moment of the star, causing it to become more aligned with the stellar equatorial plane as it settled into its final, short-period orbit¹³. The final state of 55 Cnc e would therefore be misaligned with the orbital planes of the outer, non-transiting planets, but aligned with the host star's spin equatorial plane as measured.

This type of system architecture for USPs is supported by previous studies. Kepler USPs in multiplanet systems have been found to have larger mutual inclinations with the other outer planets 10 . Recent analysis of HD 3167 b, an ultra-short-period super-Earth

$$(P = 0.959641 + 1.1 \times 10^{-5}; M_p = 5.02 \pm 0.38 M_{\oplus})$$
, and HD 3167 c, a

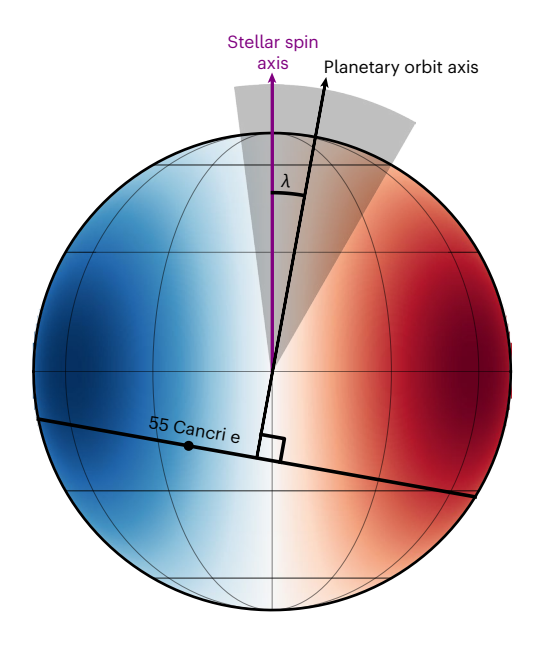


Fig. 2 | A visual representation of the sky-projected alignment between 55 Cnc e's stellar spin axis and planetary orbit axis. The apparent Doppler shift of the star's surface that arises from its rotation is shown in shades of blue to red, which correspond to the degree to which the stellar surface appears blue- or redshifted. Lighter shading corresponds to smaller Doppler shift. The star is shown with an inclination $i_* = 90^\circ$, which is consistent with the wide constraints on our estimate of i_* . The 1σ confidence level for 55 Cnc e's orbit axis is shown by the grey shading. The transit trajectory is shown as a black band. The size of the planet is to scale with the size of the star.

sub-Neptune on a 30 day period, returned a similar system architecture ^{23,29}. The inner USP, HD 3167 b, was found to have an orbit normal closely aligned with its host star's spin axis (ψ = 29.5 $^{+7.2^{\circ}}_{-9.4^{\circ}}$) while the further out planet, HD 3167 c, has an orbit nearly perpendicular to the orbit of HD 3167 b (ψ = 107.7 $^{+5.1^{\circ}}_{-4.9^{\circ}}$). We find that 55 Cnc similarly has a USP, 55 Cnc e, with an orbit aligned with the stellar equatorial plane although the alignment of the outer planets are unclear since they do not transit.

The close alignment of the ultra-short-period, super-Earth 55 Cnc e's orbit normal with its host star's spin axis places constraints on theories for how USPs migrate to their present day positions and how they interact with other planets in compact multiplanet systems. This measurement additionally gives clues as to why none of the other known planets around 55 Cnc transit and the possible role of 55 Cnc's distant stellar companion. This small-amplitude RM measurement of a super-Earth is only now achievable because of new, ultra-stabilized spectrographs capable of delivering sub-metre-per-second precision. More spin-orbit alignment measurements of USPs will help us to understand this unique population of planets and the nature of the planetary tidal dissipation that causes them to migrate so close in to their host stars.

Methods

Photometric data and transit fit

TESS observed 55 Cnc at a 2 min cadence during Sector 21 (21 January to 18 February 2020) and a 20 s cadence during Sector 44 (12 October to 5 November 2021) and Sector 46 (3 December to 30 December 2021). We use the publicly available light curves that have been detrended of common instrumental systematics 30 . We found evidence of high-frequency correlated noise throughout the first sector (Sector 21) of observations

and therefore use only the later two sectors (that is, Sectors 44 and 46) with 20 s exposure times. In total, we used 199,838 TESS cadences of 55 Cnc.

Both sectors of TESS data are fit for simultaneously with a Hamiltonian MCMC method implemented using exoplanet, PyMC3 and Theano^{31–33}. The fit is parameterized using the stellar mass and radius rather than just the stellar density, since the planet has a low eccentricity and there exists direct interferometric constraints on the stellar radius of 55 Cnc³⁴. The Gaussian priors for the stellar mass and radius are given in Supplementary Table 1. We additionally fit for the orbital period, P, transit mid-time, T_0 , planet-to-star radius ratio, R_p/R_\star , and impact parameter, b. Each sector is also fit to an independent Gaussian process (GP) model using a Matérn-3/2 kernel parameterized by an amplitude $\sigma_{\rm GP}$ and a timescale $\tau_{\rm GP}$ to account for any background variations in the light curve ^{35,36}. The model also includes a mean flux and a white noise term to inflate the photon noise uncertainties from TESS.

The model included quadratic limb darkening, with coefficients determined using the LDTk code package³⁷. This code uses the PHOE-NIX stellar atmosphere models³⁸ to generate observed disk intensities based on the TESS bandpass and input stellar parameters $T_{\rm eff}$, Fe/H and $\log g$ that were obtained from spectroscopic analysis (Supplementary Table 1). The limb-darkening coefficients were fit for as part of the model and were constrained using Gaussian priors, though the uncertainties were inflated by a factor of five to account for the uncertainties in the stellar model. We ran two independent chains for 1,500 tuning steps and 1,000 production steps. We verified that convergence was reached by making sure the \hat{R} metric, as defined in Gelman et al.³⁹, was below a conservative 1.001 threshold. We additionally ensured that the effective number of samples per parameter was >200. The TESS data and best-fit transit model is shown in Supplementary Fig. 1. The resultant transit fit parameters, which agree with literature values^{8,40,41}, are given in Table 1 with the GP parameters given in Table 2.

Spectroscopic data

EXPRES observed 55 Cnc e during transit on 31 January 2022 (28 observations) and 6 April 2022 (27 observations). EXPRES is a stabilized, next-generation, optical (390–780 nm) spectrograph with a high median resolving power of $R \approx 137,000$ (ref. 19) mounted on the 4.3 m Lowell Discovery Telescope (LDT) 42 . It has a measured instrument stability of 3–7 cm s $^{-1}$ and returns an intranight scatter of 10–40 cm s $^{-1}$ on-sky for select quiet stars 43,44 .

EXPRES observations were terminated after they reached an SNR of 225, which corresponds to a resultant analytical RV error of approximately 35 cm s $^{-1}$ (ref. 45). Most observations took between 4 and 9 min. The last five observations on 6 April 2022, which fall after the transit, required longer exposure times of 15–17 min to reach the target SNR as the weather quickly degraded. RVs are derived using a template-matching, chunk-by-chunk technique. These RV measurements are given in Supplementary Table 2.

55 Cnc stellar properties

We also use the EXPRES spectra to derive stellar properties of $55\,\mathrm{Cnc}^{20}$. The analysis uses the forward modelling tool, SME²¹, to fit both the global stellar properties and individual abundances of $15\,\mathrm{elements}$ using more than $7,000\,\mathrm{atomic}$ and molecular lines over ~350 Å of spectrum. The method first fits for T_{eff} , $\log g$, rotational broadening and a scaled solar abundance pattern [M/H], with only calcium, silicon and titanium allowed to vary independently. The temperature of this model is perturbed $\pm 100\,\mathrm{K}$ and the parameters are re-derived. The global parameters are then fixed to those found while the abundances of $15\,\mathrm{elements}$ (C, N, O, Na, Mg, Al, Si, Ca, Ti, V, Cr, Mn, Fe, Ni and Y) are allowed to vary. These steps are then repeated, this time starting with the newly derived abundance pattern. Finally, a temperature and gravity dependent macroturbulence is assigned and we solve for $v\sin i_*$ with all other parameters fixed.

In total, 290 EXPRES 55 Cnc spectra were analysed in this way; the χ^2 weighted averages adopted for the parameters can be found in Supplementary Table 1. The distribution of returned model parameters gives us a measure of the model fit for this star but does not take into account the uncertainties in the model itself. The standard deviations in the returned $T_{\rm eff}$, $\log g$ and $v \sin i_{\star}$ values were 5 K, 0.015 dex and 0.05 km s⁻¹, respectively. We therefore adopt the larger uncertainties that take into account model uncertainties across a range of stellar parameters²⁰.

RM fit

We model the RM signal in the EXPRES RV data using ellc^{46,47}. The emcee ensemble sampler is used to perform MCMC sampling to find the range of parameters compatible with the data⁴⁸. In the MCMC sampling, we allow the projected stellar rotation, $v\sin i_{\star}$, and sky-projected stellar obliquity, λ , to vary uniformly in the range 0–20 km s⁻¹ and –180° to 180°, respectively. By using uniform priors for $v\sin i_{\star}$ rather than priors based on the value determined by SME, we are able to get independent measures of $v\sin i_{\star}$ from both SME and the RM fit.

For each transit, our model includes a white noise term to inflate the photon noise uncertainty as well as a linear model with parameters y_0 (intercept) and m (slope) to account for the stellar reflex motion due to the orbiting planets. The slope is a free parameter that is fit to the out-of-transit data at every step in the MCMC method. The intercept is then determined from a weighted average of the out-of-transit residuals after subtracting the slope.

The transit also gives rise to a second RV anomaly due to turbulent convective motion on the surface of the star⁴⁹. We include a model for the convective blueshift variation⁵⁰ and assume a net convective blueshift centred on $V_{CB} = -150 \text{ m s}^{-1} \text{ (refs.}^{51,52})$ with a standard deviation of 100 m s⁻¹. The contribution of the convective blueshift model has a semi-amplitude of 1.3 cm s⁻¹ and is shown as a grey dotted line in Fig. 1.

The orbital period P, transit time t_0 , scaled separation a/R_\star , radius ratio r/R_\star and orbital inclination i are updated in every step of the MCMC method by sampling from a multivariate normal distribution, the mean and covariance properties of which are determined from the posterior distribution obtained from the TESS analysis. This effectively places Gaussian priors on the transit parameters, but also takes into account their covariance.

We ran an ensemble of 300 emcee 'walkers' for 2000 steps each, discarded 750 samples as a burn-in, thinned the chains by the autocorrelation length and finally merged the chains together to obtain 3,300 independent samples. The median values and 68% confidence interval for the fit for RM parameters are reported in Table 1. The range of models compatible with the data to the 99th percentile are illustrated in Fig. 1 by the yellow shading.

The RM effect is only able to measure the sky projection of the stellar obliquity, λ . The three-dimensional obliquity, ψ , can be recovered using an independent measurement of the inclination of the star,

 i_{\star} . We derive an estimate of $i_{\star} = 75 {+11^{\circ} \atop -17^{\circ}}$ by combining measurements

of the stellar radius R_{\star} , stellar rotation period $P_{\rm rot}$ and the projected rotation $v \sin i_{\star}$ from the RM fit⁵³. The distribution of i_{\star} is broad, but there is a preference for a somewhat inclined star, where $i_{\star} = 90^{\circ}$ means the spin angular momentum vector is perpendicular to our line of sight. The combination of i_{\star} , λ and orbital inclination i gives a de-projected

stellar obliquity of $\psi = 23^{+15^{\circ}}_{-12^{\circ}}$, which is consistent with a prograde, low stellar obliquity orbit for 55 Cnc e.

Our detection of a RM effect is statistically supported. Our best-fit value of $v \sin i_{\star}$ over its corresponding error is 4.3σ . We implement leave-one-out cross-validation to compare the RM model with the null hypothesis of no detection, that is a straight line 54 . This returns a χ^2 of 70.3 for an RM model versus 86.9 for a model without RM, implying that the RM model better predicts the 'unseen' left out data and is

therefore the better choice of model. The Bayesian information criterion based on the maximum likelihood fit to the full data set also favours the RM model over a straight line by 8.5, where a difference greater than 6 is typically considered significant⁵⁵.

We use GP regression bootstrapping to establish a false alarm probability for our measured RM effect. We generate 1,000 random pairs of data samples using a GP with a Matérn-3/2 covariance function whose hyperparameters are set to reflect the noise properties of the observed EXPRES data. These data have no injected RM signal as the samples have been drawn from the prior distribution over datasets. Of these realizations, only 0.3% return a best-fit RM model with a solution consistent with the RM fit with the real data, illustrated by the yellow contour in Supplementary Fig. 2. Our detection therefore has a false alarm probability of 0.3%.

Data availability

The EXPRES radial velocities used in this study are published as part of the Supplementary Information. The TESS data used in this study are publicly available and can be obtained from the Mikulski Archive for Space Telescopes (MAST; https://archive.stsci.edu/missions-and-data/tess).

Code availability

The code associated with this work used only open source software. This research made use of SciPy 56 , NumPy 57,58 , Astropy 59,60 , lightkurve 61 , starry 62 , emcee 48 , celerite 35,36 , ellc 47 and LDTk 37 . This research also made use of exoplanet 31 and its dependencies $^{32,33,59,60,62-64}$.

References

- Butler, R. P., Marcy, G. W., Williams, E., Hauser, H. & Shirts, P. Three new '51 Pegasi-type' planets. Astrophys. J. Lett. 474, L115–L118 (1997).
- Marcy, G. W. et al. A planet at 5 AU around 55 Cancri. Astrophys. J. 581, 1375–1388 (2002).
- 3. McArthur, B. E. et al. Detection of a Neptune-mass planet in the ρ^1 Cancri system using the Hobby-Eberly telescope. *Astrophys. J. Lett.* **614**, L81–L84 (2004).
- Fischer, D. A. et al. Five planets orbiting 55 Cancri. Astrophys. J. 675, 790–801 (2008).
- Winn, J. N. et al. A super-Earth transiting a naked-eye star. Astrophys. J. Lett. 737, L18 (2011).
- Demory, B.-O. et al. Detection of a transit of the super-Earth 55 Cancri e with warm Spitzer. Astron. Astrophys. 2, 17.04 (2011).
- Dawson, R. I. & Fabrycky, D. C. Radial velocity planets de-aliased: a new, short period for super-Earth 55 Cnc e. Astrophys. J. 722, 937–953 (2010).
- Bourrier, V. et al. The 55 Cancri system reassessed. Astron. Astrophys. 619, A1 (2018).
- Steffen, J. H. & Coughlin, J. L. A population of planetary systems characterized by short-period, Earth-sized planets. *Proc. Natl Acad. Sci. USA* 113, 12023–12028 (2016).
- Dai, F., Masuda, K. & Winn, J. N. Larger mutual inclinations for the shortest-period planets. Astrophys. J. Lett. 864, L38 (2018).
- Petrovich, C., Deibert, E. & Wu, Y. Ultra-short-period planets from secular chaos. Astron. J. 157, 180 (2019).
- Pu, B. & Lai, D. Low-eccentricity migration of ultra-short-period planets in multiplanet systems. *Mon. Not. R. Astron. Soc.* 488, 3568–3587 (2019).
- Millholland, S. C. & Spalding, C. Formation of ultra-short-period planets by obliquity-driven tidal runaway. Astrophys. J. 905, 71 (2020).
- Triaud, A. H. M. J. in Handbook of Exoplanets (eds Deeg, H. J. & Belmonte, J. A.), Springer International Publishing AG, 2 (2018).
- Albrecht, S. H., Dawson, R. I. & Winn, J. N. Stellar obliquities in exoplanetary systems. *Publ. Astron. Soc. Pac.* 134, 82001 (2022).

- Bourrier, V. & Hébrard, G. Detecting the spin-orbit misalignment of the super-Earth 55 Cancri e. Astron. Astrophys. 569, A65 (2014).
- López-Morales, M. et al. Rossiter-McLaughlin observations of 55 Cnc e. Astrophys. J. Lett. 792, L31 (2014).
- Pepe, F. et al. ESPRESSO—An Echelle SPectrograph for Rocky Exoplanets Search and Stable Spectroscopic Observations. Messenger 153, 6–16 (2013).
- Jurgenson, C. et al. in Ground-based and Airborne Instrumentation for Astronomy VI Vol. 9908 of Proc. SPIE, 99086T (eds Evans, C. J., Simard, L. & Takami, H.) (SPIE, 2016).
- Brewer, J. M., Fischer, D. A., Valenti, J. A. & Piskunov, N. Spectral properties of cool stars: extended abundance analysis of 1,617 planet-search stars. *Astrophys. J. Suppl.* 225, 32 (2016).
- Piskunov, N. & Valenti, J. A. Spectroscopy made easy: evolution. Astron. Astrophys. 597, A16 (2017).
- Kunovac Hodžić, V., Triaud, A. H. M. J., Cegla, H. M., Chaplin, W. J. & Davies, G. R. Orbital misalignment of the super-Earth π Men c with the spin of its star. Mon. Not. R. Astron. Soc. 502, 2893–2911 (2021).
- Bourrier, V. et al. The Rossiter-McLaughlin effect revolutions: an ultra-short period planet and a warm mini-Neptune on perpendicular orbits. Astron. Astrophys. 654, A152 (2021).
- Valenti, J. A. & Fischer, D. A. Spectroscopic Properties of Cool Stars (SPOCS). I. 1040 F, G, and K dwarfs from Keck, Lick, and AAT planet search programs. Astrophys. J. Suppl. 159, 141–166 (2005).
- 25. Kaib, N. A., Raymond, S. N. & Duncan, M. J. 55 Cancri: a coplanar planetary system that is likely misaligned with its star. *Astrophys. J. Lett.* **742**, L24 (2011).
- Hansen, B. M. S. & Zink, J. On the potentially dramatic history of the super-Earth ρ 55 Cancri e. Mon. Not. R. Astron. Soc. 450, 4505–4520 (2015).
- Boué, G. & Fabrycky, D. C. Compact planetary systems perturbed by an inclined companion. II. Stellar spin-orbit evolution. Astrophys. J. 789, 111 (2014).
- Boué, G. & Fabrycky, D. C. Spin-orbit angle in compact planetary systems perturbed by an inclined companion. Application to the 55 Cancri system. In Complex Planetary Systems, Proceedings of the International Astronomical Union Vol. 310, 62–65 (Cambridge Univ. Press, 2014).
- Christiansen, J. L. et al. Three's company: an additional non-transiting super-Earth in the bright HD 3167 system, and masses for all three planets. Astron. J. 154, 122 (2017).
- Jenkins, J. M. Advances in the Kepler Transit Search Engine. IAU Focus Meet. 29A, 210–212 (2016).
- Foreman-Mackey, D. et al. exoplanet-dev/exoplanet v.0.4.0 Zenodo https://doi.org/10.5281/zenodo.1998447 (2020).
- Salvatier, J., Wiecki, T. V. & Fonnesbeck, C. Probabilistic programming in python using pymc3. PeerJ Computer Sci. 2, e55 (2016).
- Theano Development Team. Theano: a Python framework for fast computation of mathematical expressions. Preprint at http://arxiv. org/abs/1605.02688 (2016).
- von Braun, K. et al. 55 Cancri: stellar astrophysical parameters, a planet in the habitable zone, and implications for the radius of a transiting super-Earth. Astrophys. J. 740, 49 (2011).
- Foreman-Mackey, D., Agol, E., Ambikasaran, S. & Angus, R. Fast and scalable Gaussian process modeling with applications to astronomical time series. Astron. J. 154, 220 (2017).
- Foreman-Mackey, D. Scalable backpropagation for Gaussian processes using Celerite. Res. Notes Am. Astron. Soc. 2, 31 (2018).
- Parviainen, H. & Aigrain, S. LDTK: Limb Darkening Toolkit. Mon. Not. R. Astron. Soc. 453, 3821–3826 (2015).
- Husser, T.-O. et al. A new extensive library of PHOENIX stellar atmospheres and synthetic spectra. Astron. Astrophys. 553, A6 (2013).

- Gelman, A., Carlin, J., Stern, H. & Rubin, D. Bayesian Data Analysis 2nd edn, Chapman & Hall/CRC Texts in Statistical Science (Taylor & Francis, 2003); https://books.google.co.uk/ books?id=TNYhnkXQSjAC
- 40. Demory, B.-O. et al. A map of the large day–night temperature gradient of a super-Earth exoplanet. *Nature* **532**, 207–209 (2016).
- 41. Kipping, D. & Jansen, T. Detection of the occultation of 55 Cancri e with TESS. Res. Notes Am. Astron. Soc. 4, 170 (2020).
- 42. Levine, S. E. et al. in *Ground-based and Airborne Telescopes IV* Vol. 8444 of Society of Photo-Optical Instrumentation Engineers (SPIE) Conference Series 844419 (eds Stepp, L. M., Gilmozzi, R. & Hall, H. J.) (SPIE, 2012).
- 43. Blackman, R. T. et al. Performance verification of the EXtreme PREcision Spectrograph. *Astron. J.* **159**, 238 (2020).
- 44. Zhao, L. L. et al. The EXPRES stellar signals project II. State of the field in disentangling photospheric velocities. *Astron. J.* **163**, 171 (2022).
- Petersburg, R. R. et al. An extreme-precision radial-velocity pipeline: first radial velocities from EXPRES. Astron. J. 159, 187 (2020).
- Ohta, Y., Taruya, A. & Suto, Y. The Rossiter-McLaughlin effect and analytic radial velocity curves for transiting extrasolar planetary systems. *Astrophys. J.* 622, 1118–1135 (2005).
- Maxted, P. F. L. Ellc: a fast, flexible light curve model for detached eclipsing binary stars and transiting exoplanets. *Astron. Astrophys.* 591, A111 (2016).
- 48. Foreman-Mackey, D., Hogg, D. W., Lang, D. & Goodman, J. emcee: the MCMC hammer. *Publ. Astron. Soc. Pac.* **125**, 306 (2013).
- Cegla, H. M. et al. Modeling the Rossiter-McLaughlin effect: impact of the convective center-to-limb variations in the stellar photosphere. Astrophys. J. 819, 67 (2016).
- 50. Shporer, A. & Brown, T. The Impact of the convective blueshift effect on spectroscopic planetary transits. *Astrophys. J.* **733**, 30 (2011).
- Meunier, N., Mignon, L. & Lagrange, A. M. Variability in stellar granulation and convective blueshift with spectral type and magnetic activity. II. From young to old main-sequence K-G-F stars. Astron. Astrophys. 607, A124 (2017).
- 52. Liebing, F., Jeffers, S. V., Reiners, A. & Zechmeister, M. Convective blueshift strengths of 810 F to M solar-type stars. *Astron. Astrophys.* **654**, A168 (2021).
- 53. Masuda, K. & Winn, J. N. On the inference of a star's inclination angle from its rotation velocity and projected rotation velocity. *Astronom. J.* **159**, 81 (2020).
- Andrae, R., Schulze-Hartung, T. & Melchior, P. Dos and don'ts of reduced chi-squared. Preprint at https://arxiv.org/abs/1012.3754 (2010).
- 55. Schwarz, G. Estimating the dimension of a model. *Ann. Stat.* **6**, 461–464 (1978).
- 56. Virtanen, P. et al. SciPy 1.0: fundamental algorithms for scientific computing in Python. *Nat. Methods* **17**, 261–272 (2020).
- Oliphant, T. NumPy: A Guide to NumPy (Trelgol Publishing, 2006); http://www.numpy.org/
- 58. van der Walt, S., Colbert, S. C. & Varoquaux, G. The numpy array: a structure for efficient numerical computation. *Comput. Sci. Eng.* **13**, 22–30 (2011).
- Astropy Collaboration. Astropy: a community Python package for astronomy. Astron. Astrophys. 558, A33 (2013).
- 60. Price-Whelan, A. M. et al. The Astropy Project: building an open-science project and status of the v2.0 core package. *Astron. J.* **156**, 123 (2018).
- 61. Lightkurve Collaboration. *Lightkurve: Kepler and TESS time series analysis in Python* (Astrophysics Source Code Library, 2018).
- 62. Luger, R. et al. starry: analytic occultation light curves. *Astron. J.* **157**, 64 (2019).

- 63. Agol, E., Luger, R. & Foreman-Mackey, D. Analytic planetary transit light curves and derivatives for stars with polynomial limb darkening. *Astron. J.* **159**, 123 (2020).
- Kipping, D. M. Efficient, uninformative sampling of limb darkening coefficients for two-parameter laws. *Mon. Not. R. Astron. Soc.* 435, 2152–2160 (2013).

Acknowledgements

These results made use of data provided by the EXPRES team using the Extreme Precision Spectrograph at the Lowell Discovery Telescope, Lowell Observatory. Lowell is a private, non-profit institution dedicated to astrophysical research and public appreciation of astronomy and operates the LDT in partnership with Boston University, the University of Maryland, the University of Toledo, Northern Arizona University and Yale University. EXPRES was designed and built at Yale with financial support from grants NSF MRI-1429365 and NSF ATI-1509436 and Yale University. Research with EXPRES is possible thanks to the generous support from grants NSF AST-2009528, NSF 1616086 and NASA 80NSSC18K0443, the Heising-Simons Foundation and an anonymous donor in the Yale alumni community. This paper includes data collected with the TESS mission, obtained from the MAST data archive at the Space Telescope Science Institute (STScI). Funding for the TESS mission is provided by the NASA Explorer Program. STScI is operated by the Association of Universities for Research in Astronomy, Inc., under NASA contract no. NAS 5-26555. V.K. and J.L. acknowledge support from NSF award nos. AST-2009501 and AST-2009343. J.M.B. acknowledges support from NASA grant nos. 80NSSC21K0009 and 80NSSC21K0571. R.M.R. acknowledges support from the Heising-Simons 51 Pegasi b Postdoctoral Fellowship.

Author contributions

L.L.Z. designed the project and drafted the manuscript. V.K. led the analysis and drafted the manuscript. S.C.M. contributed to the scientific interpretation. C.H. processed the TESS data. L.L.Z., J.M.B., J.L., A.E.S., R.M.R., S.H.C.C., S.A.W. and D.A.F. are members of the

EXPRES team that built and commissioned EXPRES, maintain the instrument for high precision work and supervise the data reduction pipeline. D.A.F. is the PI of the EXPRES Team and derived the EXPRES RVs. J.M.B. ran the stellar parameter analysis. L.L.Z., V.K., J.M.B., J.L., S.H.C.C., S.A.W. and D.A.F. contributed to the EXPRES observations.

Competing interests

The authors declare no competing interests.

Additional information

Supplementary information The online version contains supplementary material available at https://doi.org/10.1038/s41550-022-01837-2.

Correspondence and requests for materials should be addressed to Lily L. Zhao.

Peer review information *Nature Astronomy* thanks Teruyuki Hirano and the other, anonymous, reviewer(s) for their contribution to the peer review of this work.

Reprints and permissions information is available at www.nature.com/reprints.

Publisher's note Springer Nature remains neutral with regard to jurisdictional claims in published maps and institutional affiliations.

Springer Nature or its licensor (e.g. a society or other partner) holds exclusive rights to this article under a publishing agreement with the author(s) or other rightsholder(s); author self-archiving of the accepted manuscript version of this article is solely governed by the terms of such publishing agreement and applicable law.

@ The Author(s), under exclusive licence to Springer Nature Limited 2022